Anal. Bioanal. Electrochem., Vol. 16, No. 6, 2024, 507-536
https://www.doi.org/10.22034/abec.2024.714076

Analytical &
Bioanalytical
Electrochemistry

2024 by CEE
www.abechem.com

Full Paper

Anti-Corrosion Performance of Ruta Graveolens Essential Oil as A Green Inhibitor for Mild Steel in 1 M HCl: Evaluations of Electrochemical, DFT And Monte Carlo

Mounir Manssouri,[1,*] Anas Chraka,[2] Ihssane Raissouni,[2] Anass Wahby,[3] and Noureddine EL Aouad[4]

[1]Research Team on Natural Products Chemistry and Smart Technologies (NPC-ST), Polydisciplinary Faculty of Larache, Abdelmalek Essaadi University, Tetouan, Morocco
[2]Materials and Interfacial Systems Laboratory, ERESI Team, Department of Chemistry, Faculty of Sciences, Abdelmalek Essaadi University, Tetouan, Morocco
[3]Laboratory of, Water, Studies and Environmental Analysis, Faculty of Sciences, Abdelmalek Essaadi University, Tetouan, Morocco
[4]Laboratory of Life and Health Sciences, Faculty of Medicine and Pharmacy, Abdelmalek Essaadi University, Tetouan, Morocco

*Corresponding Author, Tel.: +212699400646
E-Mail: man.mounir@yahoo.fr

Received: 26 April 2024 / Received in revised form: 22 June 2024 /
Accepted: 22 June 2024 / Published online: 30 June 2024

Abstract- Environmental issues have received considerable attention in recent years, and the use of green corrosion inhibitors has become the main topic of most researchers. The current study was focused on evaluating the essential oil from aerial parts of the Ruta Graveolens L. (RG-(EO)) has been used as an eco-friendly corrosion inhibitor on Mild Steel (MS) at 1 M HCl solution. The characterization method (i.e., gas chromatography-mass spectrometry (GC/MS)) identified 21 constituents representing 95.3% of the total amount and undecan-2-one (U2ONE) has been identified as the main constituent of RG-(EO). The inhibiting effect of RG-(EO) on the corrosion of MS in 1 M HCl solution was tested by the measurements of Weight loss (WL), potentiodynamic polarization (PDP), electrochemical impedance spectroscopy (EIS) as well as quantum chemical calculation methods. The PDP test findings showed that the effectiveness of MS inhibition increased with the addition of the RG-(EO), reaching almost 94.80% at 2.00 g/L. The thermodynamic analysis showed that the inhibition efficiency increases slightly with an increase in the temperature of the medium (308-343 K). Moreover, the thermodynamic kinetic parameters showed that the adsorption of RG-(EO) on MS surface sites is subject to the Langmuir adsorption isotherm. Finally, the theoretical studies based on quantum chemical analysis (i.e. density functional theory (DFT)) and Monte Carlo (MC) simulation were also performed for understanding the adsorption mechanism of U2ONE onto Fe-surface.

Keywords- Corrosion inhibitors; Ruta Graveolens L; Electrochemical methods; Undecan-2-one; Monte Carlo simulation; DFT

---

1. INTRODUCTION

MS is an extensively employed metallic material in many industries such as electrochemical technologies , the oil industry and heat exchangers etc. due to its good mechanical strength and relatively low price, but it is susceptible to several forms of corrosion in some environments, especially in the acidic medium [1,2] . Dilute hydrochloric acid is extensively used in various industries for descaling, anticoagulants, heating boilers and acid cleaning etc. [3].This phenomenon can be minimized or delayed by various means such as coatings, cathodic protection, and corrosion inhibitors [4] . Almost all inhibitors of corrosion are synthetic organic compounds. Owing to the high cost, toxicity, and dangerous effects of synthesized corrosion inhibitor [5,6], the search for green alternatives that are environmentally friendly inhibitors (i.e. biodegradable molecules) and nontoxic to protect health and insure human security is at the present time interesting [7,8]. The essential oils (EOs) and extracts components from a variety of plants origins as eco-friendly sources of sustainable corrosion inhibitors [9-14]. These types of inhibitors, which are readily available through a simple extraction process, are able and effective to protect the metal from corrosion [15,16].

Recently, a great deal of research has been carried out to study inhibitive effect several plant extract on the corrosion of steel in 1.0 M HCl [17,18]. In this context, Ammodaucus leucotrichus essential oil has been established, as an ecofriendly corrosion inhibitor of acid corrosion of MS in 1 M HCl [19]. This behavior was attributed to the adsorption of the oil molecules on the metal surface. The chemical composition of this EO analyzed by GC and GC–MS was strongly dominated by peryllaldehyde (PER) which represents 73.5%; and thus, the inhibition action of this oil can be attributed to the adsorption of this aldehyde [18].

In this study, our focus is chiefly put on essential oil of Ruta Graveolens L. Several studies revealed that R. graveolens L. chemical compounds have significant antibacterial and antifungal activity properties [20,21]. The plant extract is also act effectively against MS corrosion 1.0 M HCl [22].

In continuation, this paper reports the effect of RG-(EO) as an environmentally friendly corrosion inhibitor for MS in 1.0 M HCl using W L, PDP and EIS methods. Moreover, the importance of the present work is not only to demonstrate the value of RG-(EO) in HCl solution as a practical ecological inhibitor achieving the highest efficiency but also to specify the main molecule (U2ONE) responsible for this part and examine it individually from other elements to prove that it is a very effective green inhibitor. To support experimental studies, we placed additional emphasis on theoretical calculations such as DFT and MC simulation.

2. EXPERIMENTAL PROCEDURE

2.1. RG-(EO) Isolation

The aerial components of *Ruta Graveolens* L. (RG) including leaves, stems and flowers were collected during the flowering stage from Morocco. After that, 100 g of fresh plant material was subject to hydrodistillation for three hours using a Clevenger-type device and following the procedure described in the European Pharmacopoeia [23].

2.2. RG-(EO) characterization

The analysis of *RG*-(EO)was carried out by GC and GC-MS according to the described methodologies in our previous work [15,24-27], using a Perkin-Elmer Autosystem XL GC apparatus. Fused-silica capillary columns (60 m×0.22 mm i.e., film thickness 0.25 µm), Rtx-1 (polydimethylsiloxane) and Rtx-wax (polyethyleneglycol). Temperature program: from 60 °C to 230 °C at 2 °C/min and then held isothermally at 230 °C for 35 min. Injector and detector temperatures were held at 280 °C. Samples were injected in the split mode (1/50), the carrier gas was H_2 (1 ml/min); the volume injected was 0.2 µl of pure oil. MS conditions: Turbo mass detector quadrupole, EI+=70 eV, acquisitions scan mass range of 35-350 Da, split: 1/80, injection volume: 0.2 µl of pure oil.

2.3. Preparation of MS segments, corrosive solutions and inhibitors

MS coupons containing 0.09 wt.% (P), 0.38 wt.% (Si), 0.01 wt.% (Al), 0.05 wt.% (Mn), 0.21 wt.% (C), 0.05 wt.% (S) and the remainder iron (Fe) were used to measure weight loss. The aggressive solution of 1 M HCl was prepared by dilution of analytical grade 37% HCl with double distilled water.

2.4. Corrosion Monitoring Techniques

2.4.1. Weight loss analysis

The steel samples underwent meticulous washing with double distilled water and air drying. Then, the initial weight of each MS segment was recorded using an analytical balance. Thereafter, the specimens were immersed in 1.0 M HCl solutions with and without different concentrations from 0.25 to 2.00 g/L of *RG*-(EO) under different temperatures of 308 to 343 K after an exposure time of six hours [28]. Inhibitory efficiency (IE_w %) is determined based on the MS corrosion rates W ($mg.cm^{-2}.h^{-1}$) according to the subsequent relationship (Eqs. 1,2) [29]:

$$W = \frac{m_f - m_i}{S.t} \qquad \text{(Eq. 1)}$$

Where (m_i) and (m_f) (mg) are the MS segment weights before and after immersion in the tested solution. (S) is the area of the MS segment (cm^2) and t is the exposure time (h).

$$IE_w\% = \frac{W - W^{'}}{W} \times 100 \qquad \text{(Eq. 2)}$$

With (W) and (W') are the MS corrosion rates in both uninhibited and inhibited solutions, respectively. The extent of the surface coverage (θ) is defined as follows (Eq. 3) [29] :

$$\theta = \frac{\%IE_w}{100} \qquad \text{(Eq. 3)}$$

2.4.2. Electrochemical (PDP and EIS) analysis

Electrochemical measurements were conducted in a conventional three-electrode electrolysis cylindrical Pyrex glass cell. The working electrode (WE) in the form of disc cut from steel has a geometric area of 1 cm^2 and is embedded in polytetrafluoroethylene (PTFE). A saturated Ag/AgCl electrode and a disc platinum electrode were used respectively as reference (RE) and counter electrodes (CE), respectively. Also, the temperature was thermostatically controlled at 308 K. The we were abraded with silicon carbide paper (grade P1200), degreased with AR grade ethanol and acetone, and rinsed with double-distilled water before use.

All electrochemical measurements were performed using a potentiostat/galvanostat (Model 263A) and the electrochemical parameters values were determined using the Volta Master 4 software. Before polarization and impedance experiments, the WE have been immersed in 1 M HCl solution with and without adding different concentrations of RG-(EO) (0.25-2 g/L) for 30 minutes to establish a steady state open circuit potential (OCP). Potentiodynamic polarization studies were plotted from -800 to +800 mV versus open circuit potential (E_{corr}) at the scan rate of 0.5 mV/sec.

Inhibitory efficiency (IE %) is determined basing on the current corrosion (i) of MS at the above conditions according to the ensuing relationship (Eq. 4):

$$IE_{PDP}\% = \frac{i - i^{'}}{i} \times 100 \qquad \text{(Eq. 4)}$$

where (i) and (i') are the corrosion current densities in the absence and the presence of inhibitor, respectively. Total charge transfer resistances R_p (without inhibitor) and R''_p (with inhibitor) were calculated from Nyquist plots by measuring the impedance difference at low and high frequencies. We maintained the above experiment conditions, and then we realized the EIS tests in the frequency series varies from 100 KHz to 10 mHz at open circuit potential with signal amplitude of 10 mV. The inhibitory efficiency (IE_{EIS} %) is designed according to (Eq. 5).

$$IE_{EIS}\% = \frac{R_p^{''} - R_p}{R_p^{''}} \times 100 \qquad \text{(Eq. 5)}$$

According to constant phase element (CPE) that accounts for the heterogeneities surface via the n coefficient [29], Z_{CPE} impedance is calculated according to the following equations (Eqs. 6,7):

$$Z_{CPE} = \frac{1}{Y_0 (j\omega)^n} \qquad \text{(Eq. 6)}$$

where (CPE_{dl}) is determined by Y_o (a constant of the CPE element), (ω) is the angular frequency($x = 2\pi f_{max}$) and (j) is the imaginary unit, and n is the phase shift, which describes in detail the level of surface inhomogeneity for integers absolute numbers ($0<n<1$) [30,31]. The double-layer capacitance (C_{dl}) is defined as follows:

$$C_{dl} = Y_0 \omega^{(n-1)} \qquad \text{(Eq. 7)}$$

where Yo is the exponent and n is the phase shift.

2.5. Computational details

2.5.1. Conceptual DFT

Currently, Numerous types of ab initio quantum chemicals approaches have been used to determine the relationship between inhibition efficiency and molecular structure in addition to computation and experimental investigations. In this study, the ab initio calculations of our inhibitor U2ONE were performed by the Gaussian 09 (G09) package [32] using the density functional theory (DFT) method in the three−parameter Lee–Yang–Parr correlation function by Becke (B3LYP) level [33] with split-valence double-zeta 6−31+ G (d, p) [34], this basic set is used because it offers precise geometry and electronic properties, as indicated by several researches [35-37]. These computations studies were conducted out in the aqueous phases on the neutral and protonated forms of the inhibitor (U2ONE and $U2ONEH^+$). the water solvent effect as described by the Polarizable Continuum Model (PCM) using the integral equation formalism variant (IEF-PCM) with (SCRF) theory [38].Without any limitation on the geometry the energies of the mentioned molecular configurations were minimized, entire intramolecular forces were reduced to zero imaginary frequency in hessian matrix. On the other hand, the Frontier Molecular Orbitals (FMOs) and Molecular Electrostatic Potential (MEP) was computed and visualized in the images. DFT is used to decide the electronic features such as the energies of highest occupied (E_{HOMO}), lowest unoccupied molecular orbital (E_{LUMO}), the ionization potential (I.P), the electron affinity (E.A) the gap energy (ΔE_{gap}), the electronegativity χ , the dipole moment, the electronic chemical potential (μ), the global hardness (η), the global softness (S), the electron- accepting power (ω+), the electro-donating power (ω-), the back donation $\Delta E_{back\text{-}donation}$, the fraction of transferred electrons (ΔN) and metal/inhibitor interaction energy ($\Delta\psi$) were calculated according to Eqs. (8–18) as indicated in the literature [10,39,40]:

$$I.P = -E_{HOMO} \qquad \text{(Eq. 8)}$$

$$E.A = -E_{LUMO} \qquad \text{(Eq. 9)}$$

$$\Delta E_{gap} = E_{LUMO} - E_{HOMO} \qquad \text{(Eq. 10)}$$

$$\chi = \frac{(I.P+E.A)}{2} \qquad \text{(Eq. 11)}$$

$$\eta = \frac{(I.P-E.A)}{2} \qquad \text{(Eq. 12)}$$

$$S = \frac{1}{\eta} \qquad \text{(Eq. 13)}$$

$$\omega^{+} = \frac{(I.P+3E.A)^2}{(16\times(I.P-E.A))} \qquad \text{(Eq. 14)}$$

$$\omega^{-} = \frac{(3I.P+E.A)^2}{(16\times(I.P-E.A))} \qquad \text{(Eq. 15)}$$

$$\Delta E_{\text{back-donation}} = -\frac{\eta}{4} \qquad \text{(Eq. 16)}$$

$$\Delta N = \frac{\Phi_{Fe} - \chi_{inhibitor}}{2(\eta_{Fe} + \eta_{inhibitor})} \qquad \text{(Eq. 17)}$$

$$\Delta\psi = \frac{(\Phi_{Fe} - \chi_{inhibitor})^2}{4(\eta_{Fe} + \eta_{inhibitor})} \qquad \text{(Eq. 18)}$$

where Φ_{Fe} is work function (4.81 eV mol^{-1}) of iron surface (Fe(110)) which is reported to have higher stabilization energy and the η_{Fe} is the absolute hardness of the iron (η_{Fe} = 0 eV mol^{-1}) [41]. The frontier molecular orbitals (FMOs) distribution, Molecular electrostatic potential (MEP)map, and Mulliken charges distribution were also calculated.

2.5.2. Monte Carlo (MC) simulation approach

To achieve a better understanding of the interaction between the studied green inhibitor molecule (U2ONE) in its neutral and protonated forms (U2ONE and U2ONEH+) onto Fe-substrate was investigated by using a MC simulation study using Material Studio 8.0 software from the BIOVIA company. The simulation of intramolecular interactions inhibitor- Fe-surface were carried out with a Fe (110) supercell of size (14×14) and a vacuum slab with (4.0 nm) thickness in a simulation box (3.4 nm × 3.4 nm × 6.8 nm) with periodic boundary conditions to simulate the current effective part of the Fe-substrate, without any arbitrary boundary effects [42,43].

In the literature, it has been reported that the selected crystalline surface Fe (110) the most stable surface among other iron surfaces such as Fe (100) and Fe (111) etc. [44,45]. Furthermore, utilizing MC simulations in gas-phase and aqueous-phase adsorption onto the Fe-substrate was investigated. To simulate the aqueous-phase, the medium was composed of 100 water (H_2O) ,as well as the neutral and protonated structures (U2ONE /U2ONEH+) of the inhibitor [46]. The MC simulations were performed using the COMPASS force field at 308 K.

3. RESULTS AND DISCUSSION

3.1. Chemical composition of RG-(EO)

The GC and GC-MS analysis allowed the identification of 21 compounds accounting for 95.3 % of the total oil (Table 1), which Undecan-2-one (82.9%) was identified as major constituent of RG-(EO) (Figure 1). Additionally, the Table 1 indicate that the some compounds like Dodecan-2-one (1.5%), E-Cinamaldehyde (1.2%), α-Turmerone (1.2%),ar-Turmerone (1.1%) Undecan-2-ol (1.0%), and Undecan-2-ol acetate (1.0%) were noticed in EO with relative percentage ≥ 1%. Hence, the dominant components of RG-(EO) were established with mass percentage as follows: one hydrocarbon monoterpenes (0.1 %), three oxygenated monoterpenes (0.4 %), four hydrocarbon sesquiterpenes (1.9%), three oxygenated sesquiterpenes (3.1%), seven nonterpenic oxygenated compounds (88.4%) and three other compounds (1.4%) (Table 1).

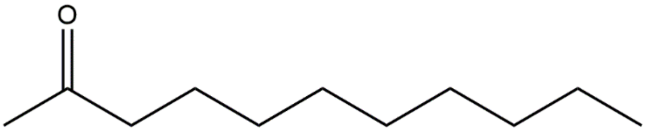

Figure 1. Chemical molecular structure of Undecan-2-one

3.2. Weight loss measurements

3.2.1. influence of RG-(EO) concentration and temperature

The results (Table 2) show that the inhibitive efficiency IE_W (%) goes up considerably with the increase in concentration of RG-(EO), indicating that the extent of inhibition depends on the concentration of this inhibitor. Besides, we notice that these findings demonstrate that the effectiveness IE_W (%) depends on the temperature and increases slightly when it rises from 308 to 343 K.

Table 1. GC and GC-MS analysis of EO composition of the RG-(EO)

N[a]	**Compounds Name**	**Ir Lit[b]**	**Ir apo[c]**	**Ir pol[d]**	**area% [e]**
1	Limonene	1025	1020	1195	0.1
2	Cineole 1.8	1024	1020	1205	0.1
3	Nonan-2-one	1074	1069	1379	0.4
4	Linalol	1086	1082	1535	0.2
5	Camphre	1123	1120	1502	0.1
6	Decan-2-one	1176	1171	1483	0.9
7	Estragole	1175	1175	1658	0.1
8	Cuminaldehyde		1212	1763	0.1
9	E-Cinamaldehyde	1234	1237	2008	1.2
10	**Undecan-2-one**	**1273**	**1279**	**1601**	**82.9**
11	Undecan-2-ol	1284	1293	1693	1.0
12	Dodecan-2-one	1381	1376	1711	1.5
13	E-Caryophyllene	1421	1416	1601	0.6
14	Undecan-2-ol acetate		1418	1655	1.0
15	α-Curcumene	1472	1469	1758	0.4
16	Tridecan-2-one	1477	1477	1797	0.7
17	(3Z.6E) -α-Farnesene	1480	1482	1762	0.3
18	Zingiberene	1489	1486	1717	0.6
19	ar-Turmerone	1643	1635	2229	1.1
20	α-Turmerone	1649	1645	2156	1.2
21	β-Turmerone		1676	2217	0.8
Total identified					**95.3**
Hydrocarbon monoterpenes					**0.1**
Oxygenated monoterpenes					**0.4**
Hydrocarbon sesquiterpenes					**1.9**
Oxygenated sesquiterpens					**3.1**
Nonterpenic oxygenated compounds					**88.4**
Others					**1.4**

Notes to Table1:

[a] Retention indices from literature on the apolar column;

[b] RI l = Retention indices on the apolar column (Rtx-1) in literature;

[c] RI a = Retention indices on the apolar column (Rtx-1);

[d] RI p = Rtention indices on the polar column (Rtx-Wax);

More than that, when the concentration reached to 2 g/L, the effectiveness (IE_W (%)) reached a high value of 95.97% in 1 M HCl solution at 343 K. Such behavior can be explained by adsorption coverage θ of RG-(EO) on the metal surface that increases with concentration of inhibitor. In the other words, we observed that the inhibitory efficiency of RG-(EO) is slightly increased when the temperature media increases, which was explained by the chemisorption behavior of RG-(EO) onto MS surface. On the other hand, we have reported, recently, that the *Ruta graveolens* leaf extract (RGE), appears to be a green corrosion inhibitor for the corrosion of MS in 1 M HCl with a maximum corrosion efficiency of 57% at 1 V/V%, after 1 day at 303 K [22]. Which indicates that RG-(EO) the best inhibitor. The distinction between RG-(EO) and RGE inhibitory effectiveness could be explained by the nature of the molecules of these inhibitors. Such behavior can be explained by adsorption coverage of RG-(EO) on the metal surface, which rises with concentration of inhibitor [47].

Table 2. Weight loss results from different concentrations of *RG*-(EO) in 1.0 M HCl at different temperatures

Temperatures	***C* (g.L^{-1})**	***W* (mg.cm^{-2}.h^{-1})**	***IE*$_w$ %**	***θ***
308 K	0.00	0.942	-	-
	0.25	0.112	88.15	0. 8815
	0.50	0.070	92.56	0. 9256
	1.00	0.064	93.18	0. 9318
	1.50	0.061	93.49	0.9349
	2.00	0.046	95.16	0. 9516
313 K	0.00	1.751	-	-
	0.25	0.204	88.37	0. 88.37
	0.50	0.128	92.68	0. 9268
	1.00	0.115	93.44	0. 9344
	1.50	0.111	93.68	0.9368
	2.00	0.080	95.45	0. 9545
323 K	0.00	2.836	-	-
	0.25	0.314	88.94	0. 8894
	0.50	0.205	92.78	0. 9278
	1.00	0.173	93.91	0. 9391
	1.50	0.171	93.96	0.9396
	2.00	0.126	95.56	0. 9556
333 K	0.00	3.641	-	-
	0.25	0.398	89.08	0. 8908
	0.50	0.261	92.83	0. 9283
	1.00	0.219	93.98	0.9398
	1.50	0.190	94.77	0. 9477
	2.00	0.151	95.86	0. 9586
343 K	0.00	6.301	-	-
	0.25	0.643	89.79	0. 8979
	0.50	0.444	92.95	0. 9295
	1.00	0.374	94.06	0. 9406
	1.50	0.328	94.79	0.9479
	2.00	0.254	95.97	0. 9597

3.2.2. Kinetic and thermodynamic parameters

Inhibitory performance as a function of temperature (T) has been discussed in this part. It is understood that the variation of the corrosion rate as a function of temperature gives results that make it possible to thermodynamically demonstrate the mechanism of RG-(EO) adsorption onto an MS surface. According to the Arrhenius plot Ln (W/T) versus 10^3/T, we calculated the enthalpy ΔH°_a and entropy ΔS°_a energies; then the standard activation E°_a was calculated from the plot of ln(W) against 10^3/T. These parameters are associated for MS without and with inhibitor basing on the following equations: Eq. 19 for ΔH°_a and ΔS°_a energies and Eq. 20 for E°_a energy [48] . The outputted parameters from the Arrhenius plot (Figures 2 and 3) are summed up in Table 3.

$$\ln\left[\frac{W}{T}\right]=\ln\left[\left(\frac{R}{N_a h}\right)+\frac{\Delta S_a^0}{R}\right]+\left[-\frac{\Delta H_a^0}{RT}\right] \qquad \text{(Eq. 19)}$$

$$\ln W=\ln A^{'}+\left[-\frac{E_a^0}{RT}\right] \qquad \text{(Eq. 20)}$$

Where W, R, T, h and N_a signify the corrosion rate, the universal constant of the ideal gas, the absolute temperature, the Plank constant and universal Avogadro number, respectively. From Table 3, we perceived that the activation standard energy attained in 1.0 M HCl with *RG*-(EO) inhibitor is lower than that when the 1.0 M HCl is alone; reflects the chemisorption of adsorption [17]. This character of adsorption can be attributed that there are electrons transfer from *RG*-(EO)molecules towards empty d-orbitals of iron atoms to form both dative and covalent bonds.

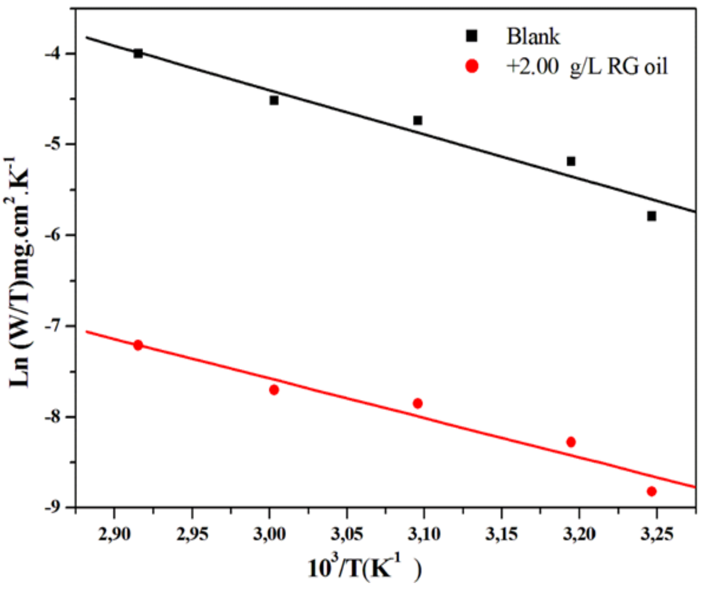

Figure 2. Arrhenius plots in 1.0 M HCl without and with *RG*-(EO) (2.00 g. L^{-1}) under various temperatures

Additionally, the positive value of standard activation enthalpy reveals the endothermic process of corrosion phenomenon of MS [49]. However, in other words, the positive value of the standard activation entropy showed a high disorder of the inhibitor molecules during adsorption [47,50].

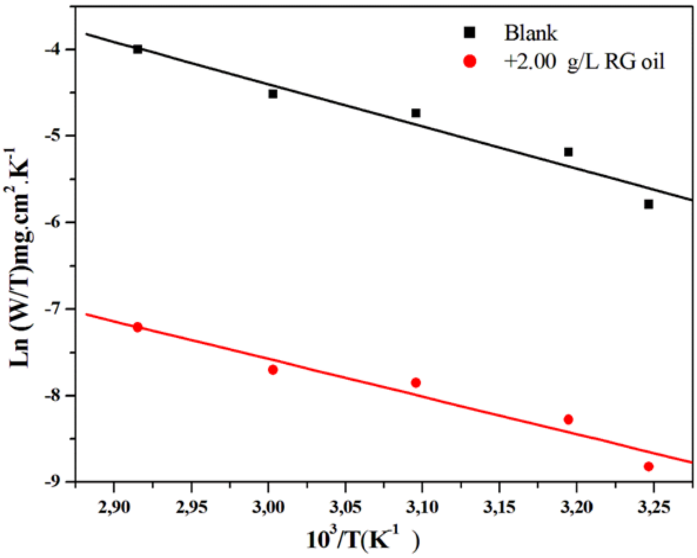

Figure 3. Transition-state plot for MS corrosion rates (W) in1.0 M HCl without and with RG-(EO) (2.00 g. L^{-1}) under various temperatures

Table 3 Kinetics thermodynamic for MS in 1.0 M HCl with and without *RG*-(EO) ((2.00 g/L)

	E$_a$ (kJ. mol^{-1})	**ΔH$_a$° (kJ. mol^{-1})**	**ΔS$_a$° (J. mol^{-1}.K^{-1})**	**Ea- ΔH$_a$ (kJ. mol^{-1})**
Blank (1.0 M HCl)	43.35	40.65	-112.29	2.70
RG-(EO) (2.00 g/L)	38.93	36.24	-151.95	2.70

3.2.3. Adsorption isotherm

To get information more about the adsorption and the surface behavior of *RG*-(EO) molecules, different models of adsorption isotherms including Langmuir, Temkin and Frumkin were considered with the range of temperature of 308 to 348 K at the different concentrations of *RG*-(EO). The equations related to these isotherms are use these formulas [51]:

Langmuir: $$\frac{C}{\theta}=\frac{1}{K_{ads}}+C \qquad \text{(Eq. 21)}$$

Temkin: $$\ln\left[\frac{C}{\theta}\right]=\ln K_{ads}-g.\theta \qquad \text{(Eq. 22)}$$

Frumkin: $$\ln\left[C.\left(\frac{\theta}{1-\theta}\right)\right]=\ln K_{ads}+g.\theta \qquad \text{(Eq. 23)}$$

where K_{ads} is adsorption coefficient, θ is the surface coverage and C_{inh} is the concentrations of the *RG*-(EO).

It is crystal clear from the data in Figure 4 attested that the straight lines of C/θ with respect to *RG*-(EO) doses C at 308 K. The linear regression factor R^2 values are showed in Figure 4. As observed in Figure 4 the values of R^2 is almost equal to 1, indicating that the adsorption on the MS surface follows the Langmuir adsorption isotherm [39]. This result suggests that the adsorbed molecules of *RG*-(EO)occupy only one protective layer and that there are no interactions between the adsorbed species [40].

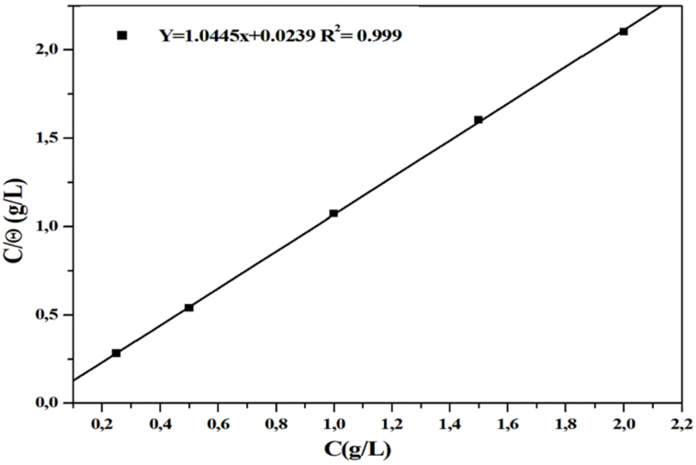

Figure 4. Langmuir adsorption isotherm of *RG*-(EO) on the MS surface in 1.0 M HCl at 308 K

3.3. Electrochemical evaluations (EIS and PDP)

3.3.1. EIS study

The inhibition performance of RG-(EO) on MS in the corrosive medium with various concentrations at 308K was studied by electrochemical impedance spectroscopy (EIS). The EIS is a very convenient and efficient approach for obtaining suitable and exact details on the adsorption of inhibitor molecules at MS/electrolyte interfaces [50,52]. The received data are depicted as Nyquist curves in Figure 5(a).

It is apparent from all Nyquist plots display one-time constant and semicircular shapes that did not change after the addition of RG-(EO). This indicates that the corrosion reaction is controlled by charge transfer, as well as the addition of the RG-(EO) did not modify the corrosion mechanism. Moreover, it appears from the Nyquist curves that an increase in the concentration of RG-(EO) led to an expansion of the diameter of the Nyquist curve. This could mean that the inhibitory substances existed in the RG-(EO) adsorbed on the active regions of the MS surface, enhancing the formation of an inhibitory film. on the other hand, the Nyquist plots were fitted using the EC-LAB program, and Figure 5(b) illustrates the equivalent electrical circuits (EEC) curve that was used to analyze the EIS data [53].

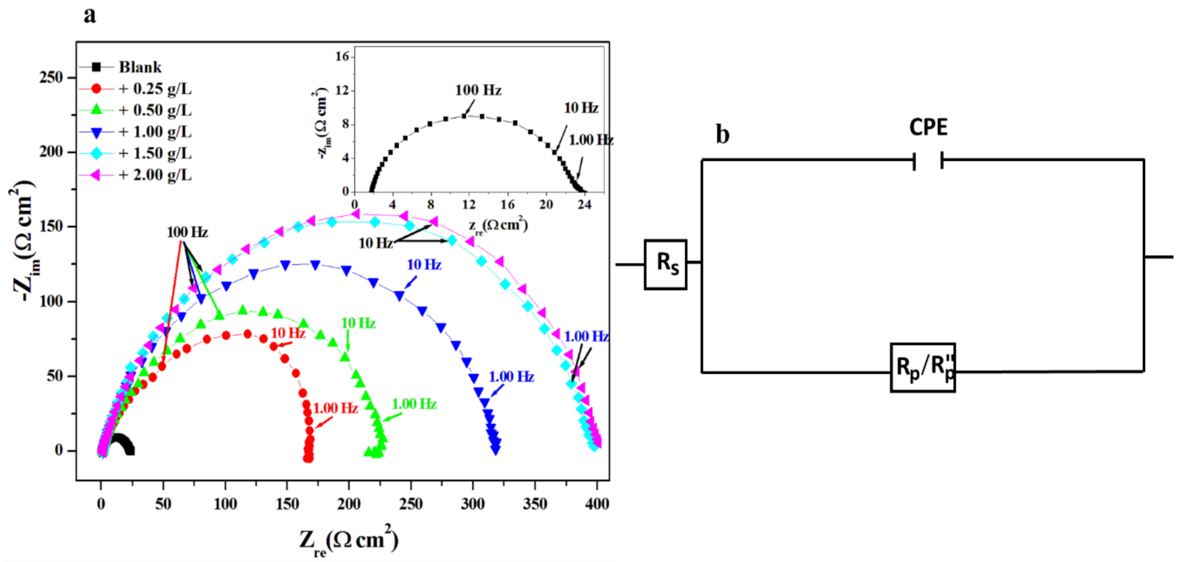

Figure 5. EIS spectra recorded for the surface of MS in 1.0 M HCl without and with different concentrations of RG-(EO) at 308 K (a) Nyquist plots; (b) Equivalent circuit used to fit the experimental EIS data

According to Figure 5(b), the EEC components consist of the (R_s), which represent the resistance of the electrolyte connected in the constant phase element (CPE_{dl}) associated with the polarization resistance (R_p/R''_p). In the absence of RG-(EO), R_p is equal to the sum of the diffuse layer resistance (R_d) and charge transfer resistance (R_{ct}) at the metal/solution interface. While in the presence of our inhibitor, that (R''_p) equals the sum of R_p, R_a (accumulated species), and R_f (film resistance). Additionally, the C_{dl} value for corrosive and inhibited approaches was calculated according to Eq.7. The capacity of the double layer for corrosion of MS in 1.0 M HCl is indicated by this parameter. Table 4 lists the corresponding values of the all-EIS parameters (R_s, R_p/R''_p, CPE_{dl} and C_{dl}) along with the inhibition efficiency (IE_{EIS}%).

Table 4. EIS parameters for MS in 1.0 M HCl containing different concentrations of RG-(EO) at 308K

C (g/L)	**R_s (Ω.cm²)**	**R_p / R''_p (Ω.cm²)**	**CPE_{dl} Y_o ($\times10^6\ S^n\ \Omega^{-1}cm^{-2}$)**	**n**	**C_{dl} ($\times10^6\ S\ \Omega^{-1}cm^{-2}$)**	**IE_{EIS} (%)**
Blank						
0.00	1.795	21.42	325	0.905	88.14	-
RG (EO)						
0.25	1.857	171.2	109.14	0.848	63.40	87.48
0.50	1.983	222	68.05	0.919	50.65	90.35
1.00	2.061	320	59.20	0.841	47.65	93.33
1.50	2.123	396.6	44.80	0.943	38.69	94.59
2.00	2.169	406.7	38.01	0.889	38.23	**94.73**

We can conclude from the data obtained about impedance (Table 4) that the C_{dl} values decreased with the increase of the concentration RG-(EO), showing that the inhibiting compounds had replaced the water molecules at the metal-corrosive medium interface [54].

According to Table 4, the values of R''_p and IE_{EIS} increased with increasing concentration of RG (EO), reaching their maximum values of 406.7 (Ω cm^2) and 94.73%. at 2.00 g/L, respectively. This may mean that in the presence of RG-(EO), the surface roughness is reduced, which contributes to reducing the iron dissolution rate by the formation of a porous protective film on the Fe-surface. Similarly, Figures 6a and 6b show the bode phase and module curves of MS in 1.0 M HCl in both uninhibited and inhibited solutions, respectively.

From Figure 6b, whether at low, mid or high frequencies, we observed that the Bode module increases with increasing RG-(EO) inhibitor concentration, indicating a good correlation with the observed IE_{EIS} of RG-(EO). further, the Bode phase curves confirm the existence of a single constant for all specimens (Figure 6b), which supported the following information: the more negative phase angle value and the more capacitive behaviour asset in the smoothing of the Fe-surface with the presence of RG-(EO) [55].

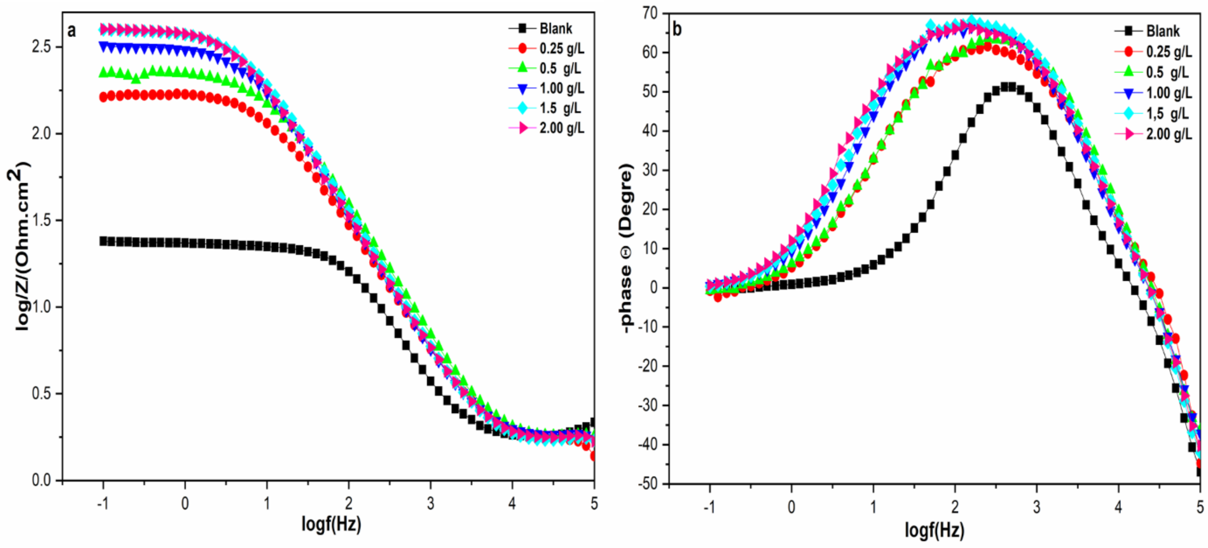

Figure 6. Bode (module (a) and phase (b)) plots of MS in 1.0 M HCl with and without different concentrations of *RG*-(EO) at 308 K

3.3.2. PDP study

It is obvious from Figure 7 that the fact of adding RG-(EO) has an inhibitive effect in both the anodic and cathodic parts of the polarization curves, revealing the mixed-type inhibition impacts of the RG-(EO). This reveals a modification of the mechanism of cathodic hydrogen evolution and anodic dissolution of steel. This of course indicates that inhibitor stops the corrosion process of MS thanks to the adsorption of an organic compound (heteroatom such as oxygen) [56].

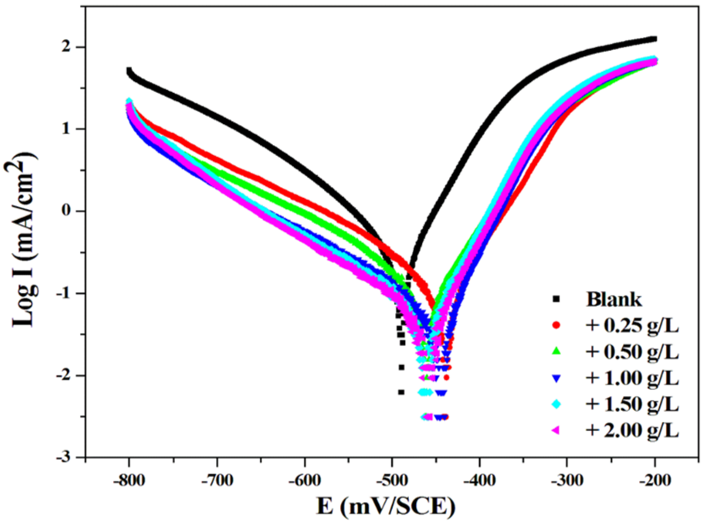

Figure 7. PDP curves of MS in 1.0 M HCl with and without RG-(EO) at various concentrations at 308 K

The corrosion potential (E_{corr}), cathodic and anodic Tafel slopes (βc, βa), and corrosion current density (I_{corr}) were all decided using the Tafel extrapolation procedure (Table 5). Table 5 show that the corrosion current densities (I_{corr}) goes down significantly with the increase of the inhibitor concentration~~,~~ suggesting that RG-(EO) inhibitory molecules efficiently deposit on the MS surface and protect the Fe-surface against corrosive attacks.

Table 5. PDP parameters of MS in 1.0 M HCl without and with different concentrations of RG-(EO) at 308K

	C (g/L)	**E_{corr} (mV/SCE)**	**I_{corr} (μA cm^{-2})**	**βc (mV dec^{-1})**	**βa (mV dec^{-1})**	**IE_{PDP} (%)**
Blank (1M HCl)		-490	578	-147.7	74	-
RG-(EO)	0.25	-460	78	-117.3	56.1	86.50
	0.50	-440	63	-102.8	54.3	89.10
	1.00	-460	35	-101.1	52.6	93.94
	1.50	-450	33	-132.8	50.8	94.29
	2.00	-430	30	-137.9	49.4	**94.80**

The observed data also suggests that the examined inhibitors molecules from RG-(EO) created the polarization blocks for the reactive sites on the Fe-surface. The formation of a protective film on the metal surface is the main cause of the improvement of the inhibition performance [54]. This means that the adsorption of organic compounds from RG-(EO) and in particular its main compound (undecan-2-one (U2ONE)) is caused not only by electrostatic interactions but also by a strong coordination bond formed between the lone-pair of heteroatoms and the empty orbital of iron [55]. The lowest corrosion rate was found among the specimens studied in the presence of 2.00 g/L of RG-(EO), showing the highest IE_{PDP} (about 94.80%) after 1 hour of immersion.

These results support the EIS and weight loss measurements and demonstrate the excellent performance of RG-(EO) as a green inhibitor in HCl medium.

3.4. Theoretical approaches

The interaction of inhibiting compounds on the metal surface can be influenced by the type and surface charge of the metal, the types of organic molecules, the charge distribution in the compound, and the type of the corrosive environment [57]. As described previously, the weight loss analysis is among the methods that provide an understanding on the thermodynamic properties of inhibitor interaction. The adsorption isotherm can offer very important information on the adsorption between the inhibitor and the metal substrate. The electrochemical measurement estimates the changes in corrosion potential and corrosion current density as well as the capacitive performance of the inhibitor layer, respectively. Additionally, an organic corrosion inhibitor may engage in neutral or protonated interaction with a corroding metal surface and can either donate or take electrons. In this area, modeling studies via Density Functional Theory (DFT) and Molecular Dynamics (MD) approach can offer a computational estimation of the electronic-scale perspective of organic corrosion inhibitors encountering physical or chemical interaction at the metal/medium interface [58,59].

3.4.1 DFT findings

3.4.1.1. Optimized structure of the molecules U2ONE, U2ONEH+

To find the most stable conformations, we first ran a conformational study on molecular structures of the neutral and protonated forms of the selected green inhibitor (U2ONE and U2ONEH+). The most stable conformations were then fully optimized.

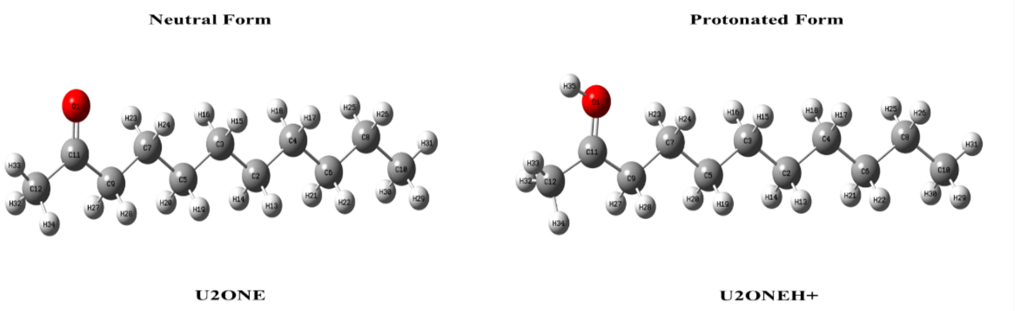

Figure 8. Optimized molecular structures of U2ONE and U2ONEH+ calculated by the DFT/B3LYP /6-31+G (d, p) in the aqueous phases

The minimized molecular structures of U2ONE and U2ONEH+ are shown in Figure 8. Additionally, the geometrical parameters of the U2ONE and U2ONEH+ including bond lengths (Å) and bond angles (°) calculated by B3LYP /6-31+G(d, p) in the aqueous phases are reported in as shown in Table 6.

Table 6. Selected optimized geometrical parameters bond lengths (Å) and bond angles (°) of U2ONE and U2ONEH+ calculated by DFT/B3LYP /6-+31G(d, p) in the aqueous phases

Bond lengths (Å)			**Bond angles (°)**		
	Cal.	**Cal.**		**Cal.**	**Cal.**
Parameter	**U2ONE**	**U2ONEH+**	**Parameter**	**U2ONE**	**U2ONEH+**
O (1)-C (11)	1.226	1.281	C(3)-C (2)-C (4)	113.64	113.54
C (2)-C (3)	1.534	1.534	C(2)-C (3)-C (5)	113.52	113.24
C (2)-C (4)	1.534	1.534	C(2)-C (4)-C (6)	113.62	113.55
C (3)-C (5)	1.534	1.534	C(3)-C (5)-C (7)	113.34	112.86
C (4)-C (6)	1.534	1.534	C(4)-C (6)-C (8)	113.69	113.67
C (5)-C (7)	1.534	1.534	C(5)-C (7)-C (9)	112.60	111.52
C (6)-C (8)	1.534	1.534	C(6)-C (8)-C (10)	113.30	113.29
C (7)-C (9)	1.529	1.530	C(7)-C (9)-C (11)	115.45	117.40
C (8)-C (10)	1.533	1.533	O(1)-C (11)-C (9)	122.16	116.65
C (9)-C (11)	1.518	1.474	O(1)-C (11)-C (12)	121.23	121.18
C (11)-C (12)	1.513	1.476	C(9)-C (11)-C (12)	116.59	122.15
			C(11)-O (1)-H (35)	-	114.20

It is crystal clear from the results of the optimized structures (Figure 8/Table 6) that the compounds U2ONE and U2ONEH+ are perfectly planar. To characterize how protonation affects the strength of the bonds, salient bond lengths in the molecules were compared between neutral and protonated forms. A comparison of bond length values in U2ONE and U2ONEH+ showed that the protonation structure (U2ONEH+) did not drastically change the bond lengths. Most changes during U2ONEH+ were observed for C (7)-C (9) and O(1)-C(11) (Table 6). It is evident that these bonds became slightly longer after protonation compared to U2ONE, whereas those of the C (9)-C (11) and C(11)-C(12) bonds became slightly shorter compared to those of U2ONEH+.

3.4.1.2. Frontier molecular orbitals and quantum reactivity descriptors of the molecules U2ONE, U2ONEH+

The frontier molecular orbitals (FMOs) HOMOs and LUMOs, Molecular electrostatic potential (MEP), as well as global reactivity descriptors are generally recognized as important parameters for specifying the activity of compounds and indicating the course of chemical processes [60,61]. The examination of FMOs and MEP maps of neutral (U2ONE) and protonated (U2ONEH+) forms of the studied green inhibitor using B3LYP/6-31+G (d,p) computations in aqueous phases are depicted in Figure 9.The HOMO map depicts the regions of compounds with a strong inclination to give electrons to electrophilic species, whereas the LUMO map depicts the regions of compounds with a strong inclination to accept electrons from nucleophilic species [61].

As seen in Figure 9, the orbitals occupied by electrons are represented by two colors, the red color indicates a greater concentration of electrons at that location, while the green indicates a deficit of electrons at that location. The molecular orbitals (HOMO) of the U2ONE are mostly located on the around the carbonyl group (C11=O1), suggesting that these are the main sites for electron donation while molecular orbitals (LUMO) of the U2ONE is majorly distributed on the atoms the around the C11=O1 moiety, as well as on the (C12) and (C9) atoms. Following protonation (U2ONEH+), there is a significant change in the position of the distribution of molecular orbitals (HOMO) which mostly emanated from the carbon atoms (C4-C6-C8). On the other hand, the level of LUMO regions remained unchanged. Indeed, when the inhibitor is protonated, its physical and chemical characteristics change, which suggesting that the protonation is responsible for the displacement of the HOMO locations of the green inhibitor. It appears from the results of the HOMOs and LUMOs distributions of the neutral (U2ONE) and protonated (U2ONEH$^+$) forms are the most likely locations for the donor-acceptor sites and therefore the optimal adsorption centers on the Fe-substrate. Within the framework of the previous concept, the molecular electrostatic potential (MEP) is a useful method to illustrate possible interaction sites on an inhibitor molecule and it uses a variety of colors to identify areas or sites with negative and positive electrostatic potentials, as well as H-binding interactions. Additionally, it helps in the visual comprehension of relative polarity of the compound. As displayed in Figure 9, the red, orange, or yellow colors (negative electrostatic potential), blue color (positive electrostatic potential) , as well as green color (zero potential) regions depict the electrophilic attack, nucleophilic attack and neutral areas in the U2ONE/U2ONEH$^+$ respectively [39]. Taking a closer look at the MEP map (Figure 9) for U2ONE reveals that the area of strong negative electrostatic potential is observed around the oxygen atom (O1) which undergoes the electrophilic attack, this explains why the (C11=O1) group acts as an electron donor site. On the other hand, the protonated form (U2ONEH+) displays only the topological feature of blue and green hues, suggesting that this format has a receiver-like effect for electrons arriving from occupied orbitals inside the Fe- surface. Based on these remarks, the neutral form (U2ONE) is most likely adsorbed via electron-rich site (C11=O1) more preferentially on the metal surface than the protonated form (U2ONEH$^+$). Further, DFT computations were also performed to explain the Physico-chemical characteristics of the U2ONE and U2ONEH+ structures to better understand their adsorption mechanisms on the Fe-surface. The various quantum parameters of neutral and protonated forms of the title molecule were calculated and listed in Table 7. Molecular reactivity was examined by analyzing frontier molecular orbital energies (E_{HOMO} and E_{LUMO}), which are critical quantum characteristics for predicting chemical reactivity and used in corrosion inhibition studies. The ability of molecules to donate electrons is directly related to the high occupied molecular orbital energy (E_{HOMO}) [62].

From Table 7, it emerges by comparing the two structures (U2ONE/U2ONEH+) of the title molecule, that U2ONEH+ had lower E_{HOMO} and E_{LUMO} values (-8.330eV and -3.296 eV) when compared to the obtained indices for U2ONE (-7.118 and -0.763 eV). This indicates that the U2ONEH$^+$ structure increases the ability to accept electrons but reduces the tendency to donate electrons from an inhibitory molecule. According to the previous conception, higher anticorrosive activity can be indicated by a smaller energy (ΔE_{gap}) gap between E_{LUMO} and E_{HOMO} [7]. The results as indicated in Table 7 reveal that the U2ONEH+ structure had a smaller ΔE_{gap} value than U2ONE (ΔE_{gap} =5.034 eV vs. ΔE_{gap} =6.355 eV), indicating that the protonated form of the title molecule can interact with Fe-surface, compared to the neutral form (U2ONE). In reality, the U2ONEH$^+$is attracted (by electrostatic interactions) towards the Fe-atoms by the already adsorbed anion [63]. Electronegativity (χ) is another important quantum descriptor that suggests an inhibitor molecule with a higher value of χ has a lower donate-transfer electron ability to the iron metal [64]. In our case, U2ONE and U2ONEH+ offers the χ values of 3.940 eV and 5.813 eV, respectively. Indicating that U2ONE is a highly reactive compound with the Fe- surface resulting in the potent inhibitory ability of U2ONE. Global hardness (η) and Chemical softness (S) are essential indices to gauge the molecular stability and reactivity of the compound [61]. The low value of η is related to high electron-donating capacity, adsorption preference, as well as inhibition efficiency, and the opposite is true for S. From the results in Table 7, U2ONEH+ had a high softness value (0.397 eV^{-1}) and a low hardness value (2.517 eV) compared to U2ONE (0.314eV^{-1}/3.177eV). These results suggest that the protonated structure is more likely to adsorb firmly on the Fe surface than the neutral structure and thus applies the best protective effect. Recently, a several authors used Electron-accepting power (ω+) and Electron-donating power (ω-) to analyze the ability of a specific system to accept - donate electrons [40,65]. It is important to note that a large value of ω+ indicates that the system has a high capacity for electron- accepting. While a lower value of ω^- indicates an effective electron donor system. the computations indicated that U2ONEH+ had a highest value of ω^+ = 4.120eV and ω^- = 9.933eV when compared to the obtained parameters for U2ONE (0.870 eV/4.810) suggesting that the U2ONEH+ structure is more capable of accepting electrons from Fe-atoms than that of U2ONE structure. In this work, the back donation ($\Delta E_{back\text{-}donation}$) was also determined. This indicator provides information on the electronic back donation methodology that can occur between the inhibitor molecule and the atoms of the metallic surface. The negative value of $\Delta E_{back\text{-}donation}$ clearly shows that the inhibitory structure has the ability to receive electrons from the Fe-surface in order to establish retro-donor bonds, which improves the efficiency of inhibition [66].

According to Table 7, $\Delta E_{back\text{-}donation}$ were found to be -0.794 and -0.629 eV for U2ONE and U2ONEH+, respectively. These values imply that these forms appear as good corrosion inhibitors with a preference for the U2ONE structure The fractions of electrons transferred (ΔN) is another factor that we may use to assess an organic corrosion inhibitor ability to share electrons [67]. It is comprehended that the positive value of this parameter (ΔN) indicates that the electron-donating ability at the Fe-surface is probable, and vice versa [68]. As shown in Table 7, The fractions of electrons transferred (ΔN) values are positive and higher for the U2ONE (0.138) compared to their U2ONEH+ (-0.197). This shows that a neutral structure is more likely to be electron-donate due to its strong reactivity with iron substrate than its protonated type, while the negative value of the protonated form (U2ONEH+) indicates that this form is unable to donate its electrons, while they have the strength of the acceptor present to a greater capacity. When analyzing the anti-corrosion capabilities of our structures (U2ONE/U2ONEH+), Metal/inhibitor interaction energy (Δψ) is a crucial factor. This ability denotes the strength of the adsorption between the inhibitor in its neutral and protonated forms(U2ONE/U2ONEH+) onto the Fe-surface. U2ONE had a low Δψ value (0.060eV) when compared with U2ONEH+(0.097 eV) indicating U2ONEH+ is a good inhibitor.

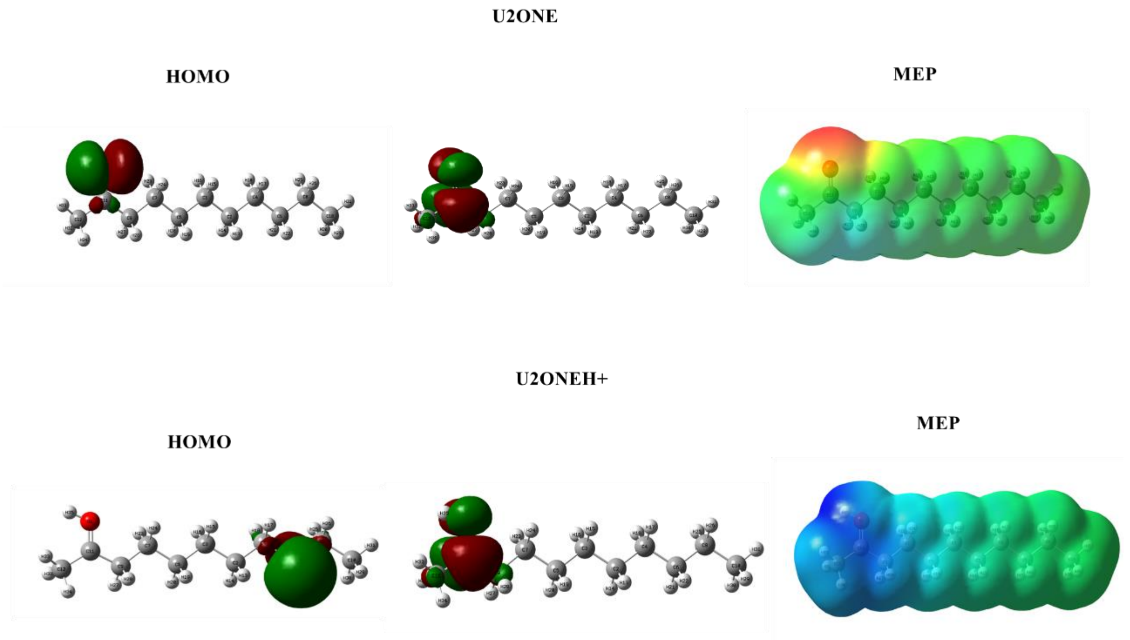

Figure 9. HOMOs, LUMOs and MEP maps for the U2ONE, U2ONEH+ in aqueous phase at DFT/B3LYP/6-31+ G (d, p) levels of theory

Table 7. The calculated global reactivity descriptors of the U2ONE, U2ONEH+ in aqueous phase at DFT/B3LYP/6-31+ G (d, p) levels of theory

Property	**DFT/B3LYP/6-31+ G (d, p)**	
	U2ONE	**U2ONEH+**
Energy of highest occupied molecular orbital (E_{HOMO}) (eV)	-7.118	-8.330
Energy of lowest unoccupied molecular orbital (E_{LUMO}) (eV)	-0.763	-3.296
Energy gap (ΔE_{gap}) (eV)	6.355	5.034
Ionization potential (I.P) (eV)	7.118	8.330
Electron affinity (E.A) (eV)	0.763	3.296
Electronegativity (χ) (eV)	3.940	5.813
Global hardness (η) (eV)	3.177	2.517
Chemical softness (S) (eV^{-1})	0.314	0.397
Electron-accepting power (ω+) (eV)	0.870	4.120
Electron-donating power (ω-) (eV)	4.810	9.933
Back donation ($\Delta E_{back-donation}$) (eV)	-0.794	-0.629
Fraction of transferred electrons (ΔN)	0.138	-0.197
Metal/inhibitor interaction energy ($\Delta\psi$) (eV)	0.060	0.097

By analyzing the frontier molecular orbitals, Molecular electrostatic potential (MEP), and all quantum descriptors of the neutral and protonated forms of the studied green inhibitor we can come to the following conclusions:

(i) The neutral form (U2ONE) can be adsorbed via donor-acceptor interactions between the carbonyl group (C11=O1) and the multiple (σ) electrons on this structure to create strong adsorption of U2ONE on the Fe-surface.

(ii) It is well known that the Fe-surface in aqueous solutions of HCl acid (H_3O^+ & Cl) carries positive charges [69], which is extremely difficult to approach by the U2ONEH+ due to electrostatic disharmony. As a result, the anions are adsorbed first and then U2ONEH+. Therefore, the adsorption of two structures (U2ONE/U2ONEH+) of the studied green inhibitor on the Fe-surface in HCl acid is a mixture of physical and chemical adsorbent.

3.4.1.3. Mulliken atomic charge distribution of the molecules U2ONE, U2ONEH+

After studying the frontier molecular orbitals (i.e. HOMO and LUMO), Molecular electrostatic potential (MEP), as well as global reactivity of the neutral and protonated forms (U2ONE/U2ONEH+) of the studied green inhibitor. The measurement of local reactivity regions is crucial because it can be used to interpret differences in reactivity between different atomic sites in an inhibitor molecule [70,71]. The Mulliken atomic charges can be used to get this information about local reactivity sites of the of the studied green inhibitor. According to the literature, the more negative the Mulliken atoms of the adsorbed areas of the inhibitor, the easier it is for the atom to donate its electron to the vacant orbital of the metal surface and preferentially adsorbs to the Fe surface, which results in a packed adsorption layer [72,73]. The Mulliken charges distribution computed for both forms (neutral and protonated) in the aqueous phase are shown in Figure 10.

It is clear from Figure 10 that the oxygen atom (O) has a region of excessive negative charge. Therefore, when interacting with the Fe surface, this atom exhibits nucleophilic behavior. Additional active sites for adsorption onto the metal surface include the negative charges that surround most carbon atoms (C). On the other hand, the carbon atom that carries a high density of positive charge (C11), can receive electrons from the electron donor regions on the iron surface. Moreover, the electron donor impact is reduced after protonation by the U2ONEH+ structure, while the attractor effect is increased by the decrease in the density of the positive charge of the carbon atom (C11) [74].

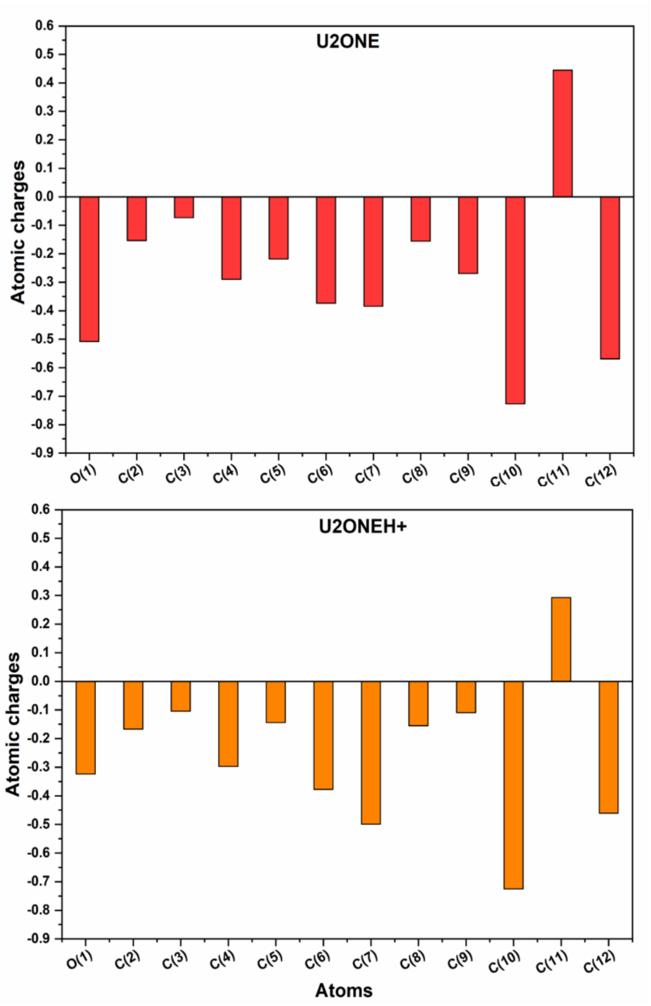

Figure 10. Graphical diagram of the Mulliken atomic charge distributions for the neutral and protonated forms (U2ONE/U2ONEH+) of the studied green inhibitor

3.4.2. Molecular simulations

In recent years, Monte Carlo (MC) Simulation has become a contemporary tool for exploring metal/inhibitor interactions [75]. The interaction properties of the studied green inhibitor in the neutral/protonated forms (i.e., U2ONE/U2ONEH+) on the Fe-surface in both the gas-aqueous phases are important main objectives during this part of our studies. Figure 11 shows the leading cells of U2ONE/U2ONEH+ on the iron (110) substrate in the gas-aqueous phases, as well as the temperature is fixed in 308K and 1 bar.

As can be seen in Figure 11, the U2ONE and U2ONEH$^+$ of the studied green inhibitor are oriented parallel to Fe-atoms in gas/aqueous phases following adsorption by a large part of the carbon (C) atoms, as well as the oxygen (O) atom. These atoms serve as reactive sites when the adsorption of the green inhibitor with the iron (110) surface. Moreover, the two structures (U2ONE/U2ONEH$^+$) of the studied green inhibitor seem to take the place of water molecules in an aqueous medium and provide a more stable location on the Fe-surface. Due to this propensity, water molecules have a synergistic impact when interacting with metallic surfaces [76,77]. In addition, the aqueous solution bind to the group (C=OH$^+$) of the protonated form (U2ONEH+) creating an ion pair onto the Fe-surface, while this is not the case for (U2ONE/100H_2O/Fe (110)) complexes. for the protonated form in HCl medium, this could result in additional stability of the studied green inhibitor as it approaches the iron (110) substrate. The current study of the adsorption systems (i.e., U2ONE/Fe (110)-U2ONEH+/Fe (110) and U2ONE/100H_2O/Fe(110)-U2ONEH+/100H_2O/Fe (110) complexes) enables effective adsorptions hence a considerable inhibitory effect referring to the experimental result. The different types of energetic descriptors of adsorbed U2ONE and U2ONEH+ in gas/ aqueous phase are calculated and listed in Table 8.

Table 8. MC simulations descriptors for the adsorption of U2ONE and U2ONEH+ in gas/ aqueous phases over the Fe (110) surface at 308 K

System	**E_{tot} (Kcal/mol)**	**E_{ads} (Kcal/mol)**	**E_{RA} (Kcal/mol)**	**E_{def} (Kcal/mol)**	**$dE_{ads}/dN_{iinhibitors}$ (Kcal/mol)**	**dE_{ads}/ dNi_{H2O} (Kcal/mol)**
Neutral						
U2ONE/Fe (110)	-146.954	-116.068	-116.068	-6.149e-^{011}	-116.068	-
U2ONE/100H_2O/Fe (110)	-896.666	-865.783	-865.783	-5.493e-^{011}	-120.272	-2.687
Protonated						
U2ONEH+/Fe (110)	-136.567	-114.676	-114.676	2.042e^{-009}	-114.676	-
U2ONEH+/100H_2O /Fe (110)	-902.138	-880.250	-880.250	1.250e^{-009}	-118,066	-3,257

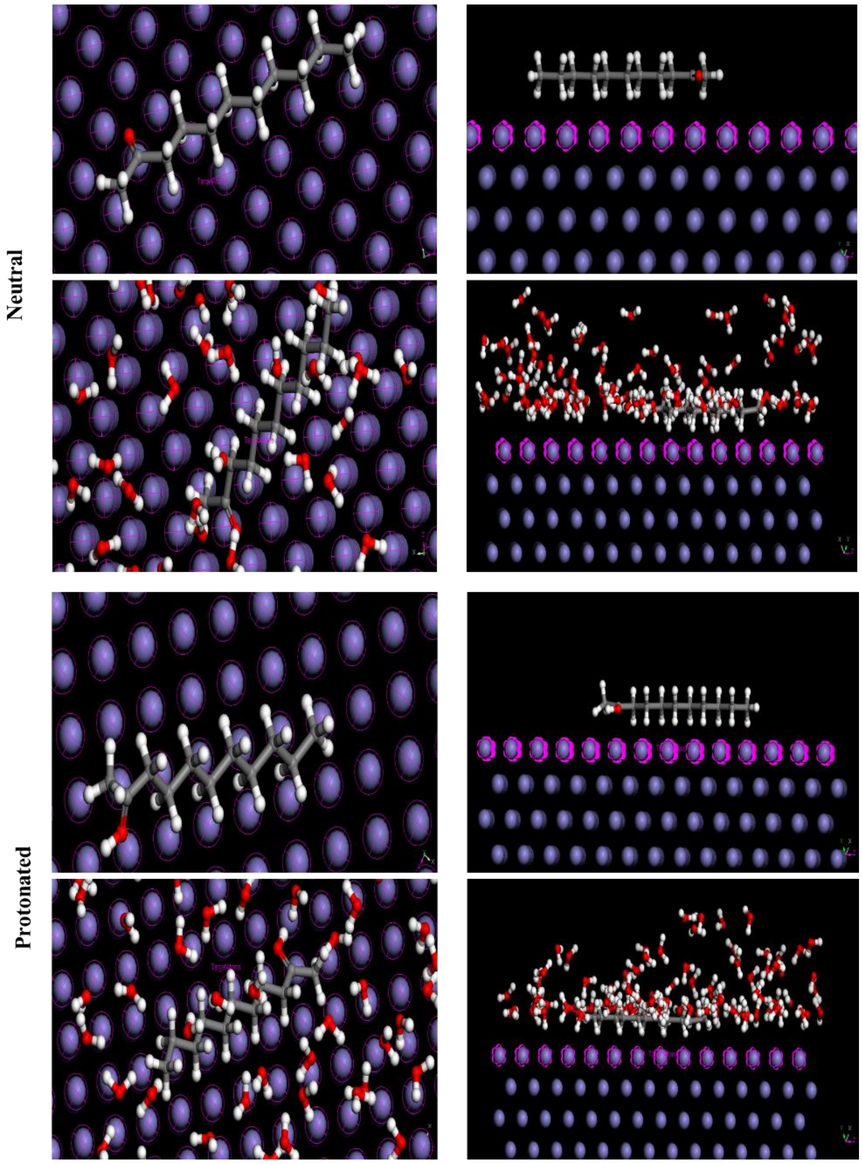

Figure 11. Upper and lateral outlooks of minimized adsorption configuration of U2ONE and U2ONEH+ in gas/ aqueous phases over the Fe (110) surface at 308 K

It is significant to mention that the higher and negative values of adsorption energy in gas phases (E_{ads}) and in aqueous phase (E''_{ads}) indicates the stable/easier adsorption onto the Fe(110) surface, as well as higher inhibition efficiency [78,79]. Moreover, the adsorption energy represents the energy absorbed when the expanded adsorbate (inhibitor) is adsorbed on the Fe-substrate [80].

It is obvious from Table 8 that the title molecule (U2ONE/U2ONEH+) in gas/solution phases interacts strongly with the iron-based layer and then forming a protective adsorbed film. Furthermore, Table 8 demonstrates that during the gas phase, E_{ads} values drop in the sequence U2ONE/Fe (110) (-116.068 kcal /mol)> U2ONEH+/Fe (110) (-114.676 kcal /mol). While the sequence changes in the aqueous phase, the decline in adsorption energies is greater: E''_{ads} fall from -880.250 Kcal/mol for U2ONEH+/100H_2O/Fe (110) and -865.783kcal/mol for U2ONE/100H2O/Fe (110). Accordingly, an aqueous solution enhances the adsorption of the green inhibitor. As indicated in the literature, this is due to the increased stability of neutral and protonated forms of the title molecule in the aqueous phase [81,82]. These impacts are particularly reinforced by the protonated form. In sum, the results of the MC reveal the anti-corrosion action capacity of the title molecule (U2ONE and U2ONEH+) in the gaseous and aqueous phases. This is totally consistent with the experiment and the DFT calculations.

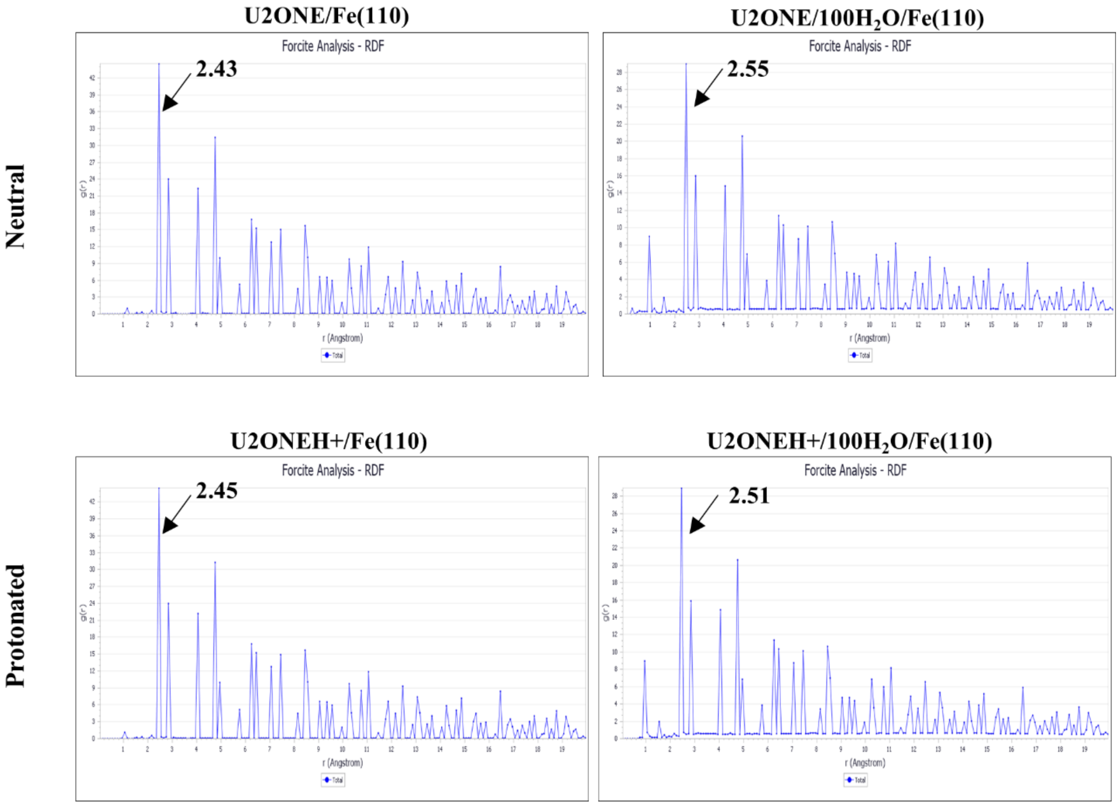

Figure 12. the RDFs of U2ONE and U2ONEH+ in gas/ aqueous phases over the Fe (110) surface at 308 K

The radial distribution function (RDF) approach based on the trajectories generated by MC Simulation is employed to define the type of bonds undertaken formed at the level of the inhibitor/Fe-substrate interface. These bonds might be either physical, chemical, or both [83]. Adsorption is normally handled by chemisorption if the bond length value is between 1-3.5 Å, while the physisorption (Van der Waals and Coulomb interactions) is normally current at a bond length value > 3.5 Å[84].

Figure 12 shows the RDF of U2ONEH+ and U2ONE in gas/solution phases. As shown in Figure 12, all the first peak values for U2ONE and U2ONEH+ in the gas/solution phases are within the chemisorption range (less than 3.55 A), While other peaks outside of 3.5 A are ascribed to physical interactions. these represent the most important interactions of the simulated structures of the title molecule on the first layer of Fe atoms, revealing that the neutral and protonated forms of the title molecule do indeed hinder the disintegration of the tested steel.

4. CONCLUSION

The first stage of this work focused on establishing the chemical composition of RG-(EO). According to GC-MS analysis, RG-(EO) has a significant concentration of U2ONE (95.3%). In the second section, we evaluated the electrochemical analyzes which showed that the RG-(EO) has proved to be able to efficiently inhibit MS corrosion in 1 M HCl solution and its inhibition efficiency values increased with increase in inhibitor concentration reaching a maximum of up to 95.16 % at 2.00 g/L at 308K. Moreover, the results of the thermodynamic activation parameters demonstrated that the studied inhibitor adsorbed on the metal surface obeyed the Langmuir isotherm model. The electrochemical studies shown by EIS and PDP (2.00 g/L) were 94.73% and 94.80%, respectively. In addition, the findings of MC simulations indicated that U2ONE in both its protonated and neutral forms is highly adsorbed onto the Fe- surface in a parallel pattern, implying higher metal surface coverage and the predicted adsorption energy correlates well with the experimental inhibitory efficiency. Through to all the experimental and computational investigations, we have discovered a new natural and effective corrosion inhibitor on mild steel in 1.0 M HCl solution: Undecan-2-one.

Authors’ statement

-Consent for publication

All authors have read and agreed to the published version of the manuscript.

-Funding

The authors did not receive support from any organization for the submitted work.

-Competing interests

The authors declare they have no conflict of interest.

-Data Availability

The datasets generated and/or analyzed during the current study are available from the corresponding author on reasonable request.

REFERENCES

[1] C. Boulechfar, H. Ferkous, S. Boufas, M. Berredjem, A. Delimi, S. Djellali, A. Djedouani, R. Bahadi, S. Laamari, K. Kumar Yadav, BH Jeon, W. Bouchelaghem, M. Alam, and Y. Benguerba, J. Mol. Struct. 1271 (2023) 134007.

[2] C. Boulechfar, H. Ferkous, A. Delimi, M. Berredjem, A. Kahlouche, A. Madaci, S. Djellali, S. Boufas, A. Djedouani, A. Errachid, A. Ali Khan, A. Boublia, T. Lemaoui, and Y. Benguerba, J. Mol. Liq. 378 (2023) 121637.

[3] C. Chai, Y. Xu, D. Li, X. Zhao, Y. Xu, L. Zhang, and Y. Wu, Prog. Org. Coat. 129 (2019) 159.

[4] H. Ferkous, A. Sedik, A. Delimi, R. Redjemia, K. Abdesalem, C. Boulechfar , A. Abdennouri , A. Madaci, M. Berredjem, A. Boublia , M. Sajid Ali , BH. Jeon, K. Ku. Yadav, Y. Benguerba, J. Mol. Liq. (2024) 123781.

[5] A. Ansari, M. Manssouri, A. Laghchimi, M. Znini, Z. Lakbaibi, and M. Azrour, Mediterr. J. Chem. 10 (2020) 62.

[6] Y.E Ouadi, M.E Fal, B. Hafezd, M. Manssouri, A. Ansari, H. Elmsellema, Y. Ramli, and H. Bendaif, Mater. Today Proc. 27 (2020) 3010.

[7] A. Chraka, I. Raissouni, N.B. Seddik, S. Khayar, A.I. Mansour, S. Tazi, F. Chaouket, and D. Bouchta, J. Bio- Tribo-Corros. 6 (2020) 1.

[8] M. Manssouri, M. Znini, Z. Lakbaibi, Y.E. Ouadi, and L. Majidi, Anal. Bioanal. Electrochem. 12 (2020) 607.

[9] A. Chraka, I. Raissouni, J. Kassout, M. Ezzaki, N. B. Seddik, F. Janoub, M. Manssouri, H. Belcadi, A.I. Mansour, and D. Bouchta, J. Mol. Liq. 392 (2023) 123507.

[10] A. Chraka, I. Raissouni, N. Benseddik, S. Khayar, A.I. Mansour, H. Belcadi, F. Chaouket, and D. Bouchta, Mater. Today Proc. 22 (2020) 83.

[11] A. Boutakiout, Z. Amrani, A. Barrahi, I. Warad, F. Benhiba, M. El Hezzat, M. Lamhamdi, M. Beraich, G. Kaichouh, A. Bellaouchou, and A. Zarrouk, Anal. Bioanal. Electrochem. 16 (2024) 227.

[12] M. Manssouri, M. Znini, Y. E. Ouadi, A. Laghchimi, M. Ouakki, and L. Majidi, Anal. Bioanal. Electrochem. 12 (2020) 944.

[13] F. Bouhlal, A. Mazkour, H. Labjar, M. Benmessaoud, M. Serghini-Idrissi, M. El Mahi, E M Lotfi, S. El Hajjaji, and N. Labjar, Chem. Data Coll. 29 (2020) 100499.

[14] Z. Akounach,A. Al Maofari,M. Damej, S. El Hajjaji, A. Berisha, V. Mehmeti, N. Labjar, M. Bamaarouf, and M. Benmessaoud, Int. J. Corros. Scale Inhib. 11 (2022) 402.

[15] M. Manssouri, M. Znini, Y. El Ouadi, A. Ansari, J. Costa, and L. Majidi, Anal. Bioanal. Electrochem. 12 (2020) 841.

[16] J. Gonzalez-Rodriguez, N. Gomez-Guzman, and J. Porcayo-Calderon, J. Bio- Tribo-Corros 7 (2021) 1.

[17] M. Manssouri, A. Laghchimi, A. Ansari, M. Znini, Z. Lakbaibi, Y. El Ouadi, and L. Majidi, Mediterr. J. Chem. 10 (2020) 253.

[18] M. Manssouri, M. Znini, Z. Lakbaibi, A. Ansari, and Y. El Ouadi, Chem. Pap 75 (2021) 1103.

[19] M. Manssouri, Y. El Ouadi, M. Znini, J. Costa, A. Bouyanzer J-M. Desjobert, and L. Majidi, Mater. Environ. Sci. 6 (2015) 631.

[20] D.N. Reddy, and A.J. Al-Rajab, Cogent. Chem. 2 (2016) 1220055.

[21] E.Z. Attia, R.M. Abd El-Baky, S.Y. Desoukey, M.A.E.H. Mohamed, M.M. Bishr, and M.S. Kamel, Future J. Pharm. Sci. 4 (2018) 254.

[22] K.K. Anupama, K.M. Shainy, and A. Joseph, J. Bio. Tribo. Corros. 2 (2016) 1.

[23] C. de l'Europe, Pharmacopée européenne, Conseil de l'Europe (1996).

[24] M. Manssouri, M. Znini, and L. Majidi, J. Taibah Univ Sci. 14 (2020) 124.

[25] M. Manssouri, A. Ansari, M. Znini, L. Majidi, and J. Costa, Egypt. J. Chem. 63 (2020) 51.

[26] M. Manssouri, A. Ansari, A. Laghchimi, M. Znini, L. Majidi, and J. Costa, J. Mater. Environ. Sci. 11 (2020) 1574.

[27] M. Manssouri, O. Ou-Ani, L. Oucheikh, A. Laghchimi, A. Ansari, L. Majidi, and M. Znini, Arab. J. Med. Aromat. Plants. 8 (2022) 41.

[28] Standard Practice for preparing, cleaning, and evaluating corrosion test specimens, Annual Book of ASTM Standards 3 (2003) 17.

[29] M. Manssouri, Z. Lakbaibi, M. Znini, Y.E. Ouadi, A. Jaafar, and L. Majidi, J. Fail. Anal. Prev. 20 (2020) 1939.

[30] C. Hsu, and F. Mansfeld, Corros. 57 (2001).

[31] M. Özcan, and İ. Dehri, Corros. Sci. 54 (2012) 201.

[32] M. Frisch, G.W. Trucks, H.B. Schlegel, G.E. Scuseria, M.A. Robb, J.R. Cheeseman, G. Scalmani, V. Barone, B. Mennucci, and G. Petersson, Gaussian 09, revision D. 01, Gaussian, Inc., Wallingford CT (2009).

[33] A.D. Becke, J. Chem. Phys 98 (1993) 5648.

[34] E. Papajak, J. Zheng, X. Xu, H.R. Leverentz, and D.G. Truhlar, J. Chem. Theory Comput. 7 (2011) 3027.

[35] S. Kerraj, M. Salah, S. Chtita, M. El Idrissi, S. Belaaouad, M. Mohammed, N. Acharjee, and N. Komiha, Comput. Theor. Chem. 1209 (2022) 113630.

[36] Ö.H. Omar, T. Nematiaram, A. Troisi, and D. Padula, Sci. Data 9 (2022) 1.

[37] M.M. Elbadawi, A.I. Khodair, M.K. Awad, S.E. Kassab, M.T. Elsaady, and K.R. Abdellatif, J. Mol. Struct. 1249 (2022) 131574.

[38] J. Tomasi, and B. Mennucci, R. Cammi, Chem. Rev 105 (2005) 2999.

[39] A. Ouaket, A. Chraka, I. Raissouni, M.A. El Amrani, M. Berrada, and N. Knouzi, J. Mol. Struct. 1259 (2022) 132729.

[40] N. Abdelshafi, M.A. Ibrahim, A.S. Badran, and S.A. Halim, J. Mol. Struct. 1250 (2022) 131750.

[41] H. Chermette, J. Comput. Chem. 20 (1999) 129.

[42] P. Singh, E.E. Ebenso, L.O. Olasunkanmi, I. Obot, and M. Quraishi, J. Phys. Chem. C 120 (2016) 3408.

[43] C. Verma, L.O. Olasunkanmi, E.E. Ebenso, M.A. Quraishi, and I.B. Obot, J. Phys. Chem. C 120 (2016) 11598.

[44] N. Asadi, M. Ramezanzadeh, G. Bahlakeh, and B. Ramezanzadeh, J. Taiwan Inst. Chem. Eng. 95 (2019) 252.

[45] L.O. Olasunkanmi, I.B. Obot, M.M. Kabanda, and E.E. Ebenso, J. Phys. Chem. C 119 (2015) 16004.

[46] E. Berdimurodov, A. Kholikov, K. Akbarov, I. Obot, and L. Guo, J. Mol. Struct. 1234 (2021) 130165.

[47] Y. Kharbach, F. Qachchachi, A. Haoudi, M. Tourabi, A. Zarrouk, C. Jama, L.O. Olasunkanmi, E.E. Ebenso, and F. Bentiss, J. Mol. Liq. 246 (2017) 302.

[48] N. Obi-Egbedi, and I. Obot, Corros. Sci. 53 (2011) 263.

[49] R. Hsissou, F. Benhiba, and S. Abbout, Chem. Commun 115 (2020) 107858.

[50] M. MANSSOURI, Y. El Ouadi, A. Chraka, M. Khaddor, M. Znini, and L. Majidi, J. Turkish Chem. Soc. 8 (2021) 953.

[51] N. Belarbi, F. Dergal, IA. El-Haci, T. Attar, D. Lerari, B. Dahmani, C.A. Ramdane-Terbouche, and K. Bachari, Anal. Bioanal. Electrochem. 13 (2021) 340.

[52] A.K. Dermani, E. Kowsari, B. Ramezanzadeh, and R. Amini, J. Ind. Eng. Chem 79 (2019) 353.

[53] R. Yıldız, Corrosion Science 90 (2015) 544.

[54] D.K. Verma, M. Kazi, M.S. Alqahtani, R. Syed, E. Berdimurodov, S. Kaya, R. Salim, A. Asatkar, and R. Haldhar, J. Mol. Struct. 1241 (2021) 130648.

[55] Z. Sanaei, M. Ramezanzadeh, G. Bahlakeh, and B. Ramezanzadeh, J. Ind. Eng. Chem. 69 (2019) 18.

[56] L. Kadiri, M. Galai, M. Ouakki, Y. Essaadaoui, A. Ouass, M. Cherkaoui, E.-H. Rifi, and A. Lebkiri, Anal. Bioanal. Electrochem. 10 (2018) 249.

[57] A. Maayta, and N. Al-Rawashdeh, Corrosion science 46 (2004) 1129.

[58] G. Gece, Corros. Sci. 50 (2008) 2981.

[59] I. Obot, D. Macdonald, and Z. Gasem, Corros. Sci. 99 (2015) 1.

[60] O. Dagdag, Z. Safi, H. Erramli, N. Wazzan, L. Guo, C. Verma, E. Ebenso, S. Kaya, and A. El Harfi, Mater. Today Commun 22 (2020) 100800.

[61] A. Chraka, I. Raissouni, N. Ben Seddik, S. Khayar, A. Mansour, H. Belcadi, F. Chaouket, and D. Bouchta, Mediterr. J. Chem. 10 (2020) 378.

[62] S. Junaedi, A.A. Al-Amiery, A. Kadihum, A.A.H. Kadhum, and A.B. Mohamad, Int. J. Mol. Sci. 14 (2013) 11915.

[63] K. Ramji, D.R. Cairns, and S. Rajeswari, Appl. Surf. Sci. 254 (2008) 4483.

[64] C. Verma, J. Haque, E.E. Ebenso, and M. Quraishi, Results Phys. 9 (2018) 100.

[65] P.S. Ganesh, G. Shimoga, S.Y. Kim, S.H. Lee, S. Kaya, and R. Salim, Microchem. J. 167 (2021) 106260.

[66] N. El-Aouni, R. Hsissou, Z. Safi, S. Abbout, F. Benhiba, J. El Azzaoui, R. Haldhar, N. Wazzan, L. Guo, and H. Erramli, Colloid Surf A Physicochem Eng. Asp. 626 (2021) 127066.

[67] M. El Faydy, F. Benhiba, I. Warad, S. Saoiabi, A. Alharbi, A.A. Alluhaybi, B. Lakhrissi, M. Abdallah, and A. Zarrouk, J. Mol. Struct. (2022) 133389.

[68] Z.L. Seeger, and E.I. Izgorodina, J. Chem. Theory Comput. 16 (2020) 6735.

[69] A. Shahmoradi, N. Talebibahmanbigloo, C. Nickhil, R. Nisha, A. Javidparvar, P. Ghahremani, G. Bahlakeh, and B. Ramezanzadeh, J. Mol. Liq. 346 (2022) 117921.

[70] R. Solmaz, G. Kardaş, M. Çulha, B. Yazıcı, and M. Erbil, Electrochim. Acta 53 (2008) 5941.

[71] H. Keleş, M. Keleş, I. Dehri, and O. Serindağ, Mater. Chem. Phys. 112 (2008) 173.

[72] J. Haque, V. Srivastava, M.A. Quraishi, D.S. Chauhan, H. Lgaz, and I.M. Chung, Corros. Sci. 172 (2020) 108665.

[73] M. Murmu, S.K. Saha, N.C. Murmu, and P. Banerjee, Corros. Sci. 146 (2019) 134.

[74] J. Saranya, F. Benhiba, N. Anusuya, R. Subbiah, A. Zarrouk, and S. Chitra, Colloid Surf A Physicochem Eng. Asp. 603 (2020) 125231.

[75] A.O. Zacharias, A. Varghese, K. Akshaya, M. Savitha, and L. George, J. Mol. Struct. 1158 (2018) 1.

[76] A. Jmiai, A. Tara, S. El Issami, M. Hilali, O. Jbara, and L. Bazzi, J. Mol. Liq. 322 (2021) 114509.

[77] S. Pareek, D. Jain, S. Hussain, A. Biswas, R. Shrivastava, S.K. Parida, H.K. Kisan, H. Lgaz, I.M. Chung, and D. Behera, Chem. Eng. Sci. 358 (2019) 725.

[78] M. Rbaa, F. Benhiba, M. Galai, A.S. Abousalem, M. Ouakki, C.H. Lai, B. Lakhrissi, C. Jama, I. Warad, and M.E. Touhami, Chem. Phys. Lett. 754 (2020) 137771.

[79] A. Jmiai, B. El Ibrahimi, A. Tara, S. El Issami, O. Jbara, and L. Bazzi, J. Mol. Struct. 1157 (2018) 408.

[80] M. Khattabi, F. Benhiba, S. Tabti, A. Djedouani, A. El Assyry, R. Touzani, I. Warad, H. Oudda, and A. Zarrouk, J. Mol. Struct.1196 (2019) 231.

[81] B. El Ibrahimi, A. Jmiai, K. El Mouaden, R. Oukhrib, A. Soumoue, S. El Issami, and L. Bazzi, J. King Saud Univ. Sci. 32 (2020) 163.

[82] M.M. Kabanda, I.B. Obot, and E.E. Ebenso, Int. J. Electrochem. Sci. 8 (2013).

[83] G. Zhang, X. Hou, B. Hou, and H. Liu, J. Mol. Liq. 278 (2019) 413.

[84] V. Mehmeti, and F.I. Podvorica, Mater. 11 (2018) 893.